

The statistical properties of spiral- and scroll-wave turbulence in cardiac tissue

K.V. Rajany,^{1,*} Anupam Gupta,² Alexander V. Panfilov,³ and Rahul Pandit^{1,†}

¹*Centre for Condensed Matter Theory, Department of Physics,
Indian Institute of Science, Bangalore 560012, India.*

²*Laboratoire de Génie Chimique, Université de Toulouse,
ENSIACET, INPT-UPS, 31030, Toulouse, France.*

³*Department of Physics and Astronomy, Gent University, Krijgslaan 281, S9, Gent 9000, Belgium[‡]*

(Dated: August 1, 2018)

Disorganized electrical activity in the heart, which is often referred to as electrical turbulence, leads to sudden cardiac death. However, to what extent can this electrical turbulence be viewed as classical, fluid turbulence, which is considered as a central problem of great importance in modern physics? In this paper we examine, for the first time, the statistical properties of electrical turbulence in two- and three-dimensional generic models of cardiac tissue by using approaches employed in studies of classical turbulence. In particular, we investigate, via extensive direct numerical simulations, the statistical properties of spiral- and scroll-wave turbulence in two- and three-dimensional excitable media by using the Panfilov and the Aliev-Panfilov mathematical models for cardiac tissue. We use very large simulation domains, and perform state-of-the-art simulations on graphics processing units (GPUs), so that we can compare the statistical properties of spiral- and scroll-wave electrical turbulence with the statistical properties of homogeneous and isotropic two- and three-dimensional fluid turbulence. We show that, once electrical-wave turbulence has been initiated, there is a forward cascade, in which spirals or scrolls form, interact, and break to yield a turbulent state that is statistically steady and, far away from boundaries, is statistically homogeneous and isotropic. For the transmembrane potential V and the slow recovery variable g , which define our models for cardiac tissue, we define $E_V(k)$ and $E_g(k)$, the electrical-wave, spectral analogs of the fluid energy spectrum $E(k)$ in fluid turbulence; and we show that $E_V(k)$ and $E_g(k)$ are spread out over several decades in k . Thus, as in fluid turbulence, spiral- and scroll-wave turbulence involves a wide range of spatial scales. Furthermore, $E_V(k)$ and $E_g(k)$ show approximate power laws, in some range of k ; unlike fluid-turbulence, the exponents for these power laws cannot, so far, be determined as accurately as their fluid-turbulence counterparts. There are diffusive terms in the equations we consider, but they do not dissipate spiral or scroll waves completely because of the excitability of the medium, so no external forcing is required to maintain these states of spiral- or scroll-wave turbulence (this is unlike fluid turbulence that requires external forcing to reach a statistically steady state). We show that for spiral- or scroll-wave turbulence the dimensionless ratio L/λ is a convenient control parameter like the Reynolds number for fluid turbulence, where L is the linear size of the simulation domain and λ the wavelength of a plane wave in the excitable medium. We calculate several other statistical properties for spiral- and scroll-wave turbulence and, by comparing them with their fluid-turbulence counterparts, we show that, although spiral- and scroll-wave turbulence have some statistical properties like those of fluid turbulence, overall these types of turbulence are special and differ in important ways from fluid turbulence.

I. INTRODUCTION

Heart disease remains the number-one, global cause of death, with 17.3 million deaths each year, according to the latest report of the American Heart Association [1]. In many cases this arises because of *sudden cardiac death*, which is a result of a cardiac arrhythmia called ventricular fibrillation (VF). Ventricular fibrillation is a result of complicated, spatiotemporal dynamics of nonlinear waves of electrical excitation in the heart.

This dynamics is associated with multiple vortices called *spiral waves*, in two dimensions, and *scroll waves*, in three dimensions. Spiral waves are found in many types of excitable media, e.g., in Belousov-Zhabotinsky-type chemical reactions [2], in the oxidation of carbon monoxide on the surface of platinum [3–5], in the propagation of calcium-ion waves in *Xenopus* oocytes [6], in the aggregation of *dictyostelium discoideum* by cyclic-AMP signalling [7, 8] and, most important, in the propagation of waves of electrical activation in cardiac tissue [9, 10].

Spiral or scroll waves in cardiac tissue tend to break down into complex spatiotemporal structures, which lead to VF, often referred as electrical turbulence [11]. It is important to study the extent to which this electrical turbulence is similar to classical, fluid turbulence, which is a problem of central importance in physics, engineering, and mathematics. Are the methods developed for studies of fluid turbulence applicable to electrical-wave turbulence in cardiac tissue? Unfortunately, we cannot answer

*Electronic address: rajany@physics.iisc.ernet.in

†Electronic address: rahul@physics.iisc.ernet.in;
also at Jawaharlal Nehru Centre For Advanced Scientific Research,
Jakkur, Bangalore, India.

‡

also at Moscow Institute of Physics and Technology (State University), Dolgoprudny, Moscow Region, Russia.

these questions based on direct experimental and clinical data as most experimental studies of turbulence require data from various space or time scales, which can differ by orders of magnitude. Fortunately, we can use alternative approaches, such as mathematical modelling and computational studies; indeed, these provide the most efficient ways for studying spiral and scroll waves and, thus, cardiac arrhythmias, in controlled *in silico* conditions [12].

Therefore, we examine, for the first time, the statistical properties of electrical turbulence in two- and three-dimensional generic models of cardiac tissue by initiating extensive, direct numerical simulations (DNSs) of spiral- and scroll-wave turbulence in very large simulation domains, in both two dimensions (2D) and three dimensions (3D), for two generic models [13, 14] for cardiac tissue; these models are used widely in cardiac research. We characterize such turbulence by using measures that are commonly used in the statistical characterization of fluid turbulence; these measures include Fourier-space spectra, probability distribution functions (PDFs) and structure functions [23].

From a general point of view we can have the following two types of homogeneous and isotropic, fully developed, 3D fluid turbulence: (A) We can have unforced, decaying turbulence, in which the energy is injected initially at large length scales L_I , i.e., into a few, low-wave-number modes ($\sim 2\pi/L_I$); this energy *cascades down to small length scales*, à la Richardson [23], until it reaches the dissipation scale η_d at which viscous losses become significant; and then the turbulence decays slowly; in this period of slow decay, fluid turbulence displays a power-law energy spectrum $E(k) \sim k^{-\alpha}$ for a long time and for the inertial range of scales $2\pi/L_I \ll k \ll 2\pi/\eta_d$; at the simplest level, the phenomenological theory [23, 24] of Kolmogorov (henceforth K41) yields $\alpha^{K41} = 5/3$, a universal exponent. (B) We can also have a statistically steady turbulence, which is an example of a driven system with a nonequilibrium statistically steady state in which the energy input, typically at large length scales L_I , is balanced by energy dissipation, which becomes significant at length scales smaller than η_d ; and, in the statistically steady state and, in the inertial range, $E(k) \sim k^{-\alpha}$, with $\alpha^{K41} = 5/3$. In addition, we discuss below, various other probability distribution functions (PDFs) and structure functions (e.g., moments of the PDF of the differences of the fluid velocity at two points) that are used to characterize this turbulent state. Furthermore, 2D fluid turbulence is qualitatively different from its 3D counterpart (see below); in particular, it displays an *inverse cascade* of energy from the injection scale L_I to large lengths and a *forward cascade* of enstrophy (the mean-square vorticity) from L_I to smaller length scales; and $E(k) \sim k^{-\alpha}$, with $\alpha = 5/3$ and $\alpha = 3$ in inverse- and forward-cascade regions, respectively.

Our goal is to explore excitable-media, spiral- and scroll-wave-turbulence analogs of 2D and 3D statistically homogeneous and isotropic fluid turbulence. Note

that there is an important qualitative difference between spiral- and scroll-wave turbulence in excitable media and fluid turbulence insofar as turbulence in an excitable medium is neither decaying nor forced. Once turbulence has been initiated in an excitable medium, e.g., by using an initial condition with a single spiral or scroll wave, we show that there is a forward cascade, which yields small spirals or scrolls; these form, interact and break all the time. The resulting turbulent state is statistically steady and, far away from boundaries, is statistically homogeneous and isotropic. For the fields V and g , we define $E_V(k)$ and $E_g(k)$, the spectral analogs of $E(k)$ in fluid turbulence; and we show that these spectra are spread out over several decades in k , i.e., like fluid turbulence, spiral- and scroll-wave turbulence involves a wide range of spatial scales; $E_V(k)$ and $E_g(k)$ show approximate power laws in some range of k , but the exponents of these do not appear to be universal. Even though there are diffusive terms in the equations we consider, they do not dissipate spiral or scroll waves completely because of the excitability of the medium. No external forcing is required to maintain these states of spiral- or scroll-wave turbulence. The only requirements are (i) a suitable initial condition and (ii) $L/\lambda \rightarrow \infty$ (or L/λ large enough in a practical calculation), where L is the linear size of the simulation domain and λ the wavelength of a plane wave in the excitable medium. The dimensionless ratio L/λ is a convenient, Reynolds-number-type control parameter (L is also used as a control parameter in a suitably scaled version of the Kuramoto-Sivashinsky equation [25]).

The remaining part of this paper is organized as follows. In Sec. II we introduce the Panfilov [13] and the Aliev-Panfilov [14] mathematical models for cardiac tissue. We then describe the numerical methods we use to study them and the statistical measures we employ to characterize the statistical properties of turbulence in these models. Section III is devoted to our results. Section IV contains our conclusions and a discussion of our results.

II. MODELS, NUMERICAL METHODS AND STATISTICAL PROPERTIES

We have used two simple, two-variable mathematical models for cardiac tissue, namely, the Panfilov and the Aliev-Panfilov models. We describe these below.

A. Panfilov model

The Panfilov model is a two-variable, Fitzgugh-Nagumo-type model, which is defined by the following partial differential equations (PDEs) for the transmembrane potential V and the slow, recovery variable g :

$$\frac{\partial V}{\partial t} = \nabla^2 V - f(V) - g; \quad (1)$$

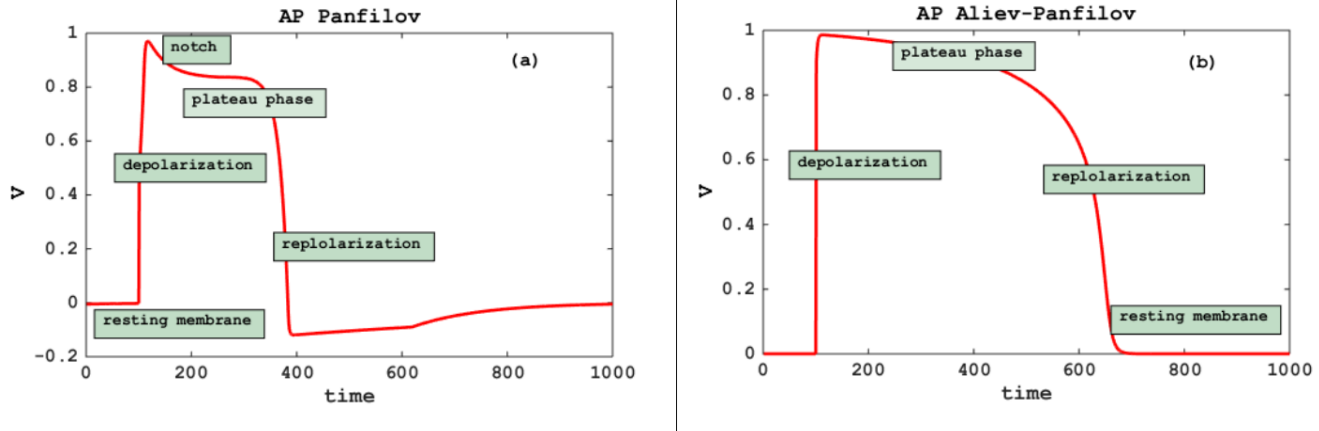


FIG. 1: Typical action potential shapes in (a) the Panfilov model and (b) the Aliev-Panfilov model. The action potential duration (APD) for the Panfilov model is 5.92 time units (time step of 0.022) and for the Aliev-Panfilov model is 42.12 time units (time step of 0.06).

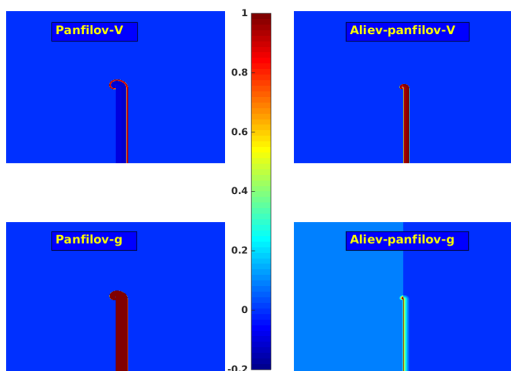


FIG. 2: Pseudocolor plots of the transmembrane potential V (top panels) and the recovery variable g (bottom panels) showing the spiral waves that we use as initial conditions for our simulations of the 2D Panfilov (left panels) and the Aliev-Panfilov (right panels) models.

$$\frac{\partial g}{\partial t} = \epsilon(V, g)(kV - g). \quad (2)$$

The initiation of the cardiac action potential is encoded in the following functional form of $f(V)$: $f(V) = C_1V$, when $V < V_1$, $f(V) = -C_2V + a$, if $V_1 \leq V \leq V_2$ and $f(V) = C_3(V-1)$, for $V > V_2$. $\epsilon(V, g) = \epsilon_1$ when $V < V_2$, $\epsilon(V, g) = \epsilon_2$ if $V > V_2$, $\epsilon(V, g) = \epsilon_3$ for $V < V_1$ and $g < g_1$; here $V_1 = 0.0026$, $V_2 = 0.837$, $C_1 = 20$, $C_2 = 3$, $C_3 = 15$, $g_1 = 1.8$, $\epsilon_1 = 0.05$, $\epsilon_2 = 1$, $\epsilon_3 = 0.3$, $a = 0.06$ and $k = 3$. The dynamics of the recovery variable is governed by $\epsilon(V, g)$: In particular, ϵ_3^{-1} specifies the recovery time constants for small V and g (its physiological

equivalent is the relative refractory period); ϵ_1^{-1} specifies the recovery time constant for relatively large values of g and intermediate values of V (its physiological equivalent is the absolute refractory period) [13]. We choose the values of the parameters, which specify this model, as in Ref. [13, 16], so that we get experimentally reasonable action potentials (APs). In this model, earlier studies [13, 16] have obtained dimensioned time by multiplying dimensionless time by 5 ms so that the spiral-wave-rotation period is $\simeq 120$ ms; and a space-scaling factor of 1 mm yields a spiral-arm wavelength of $\simeq 32.5$ mm; the dimensioned value of the conductivity constant has been chosen to be $2\text{cm}^2/\text{s}$. In this paper, we express all times in terms of the action-potential duration (APD). The action potential (AP) for the Panfilov model is shown in Fig. 1(a). The action potential duration (APD) for the Panfilov model is 5.92 time units (time step of 0.022).

B. Aliev-Panfilov model

Each site in the Aliev-Panfilov mathematical model for cardiac tissue [14] is described by the following coupled equations for the transmembrane potential V and the variable g , which represents the conductance of the slow inward current:

$$\frac{dV}{dt} = -kV(V - a)(V - 1) - Vg + I_{ex}; \quad (3)$$

$$\frac{dg}{dt} = \left[\epsilon + \frac{\mu_1 g}{\mu_2 + V} \right] [-g - kV(V - b - 1)]; \quad (4)$$

I_{ex} is the external current from all neighboring cells. The first term in Eq. (3) determines the fast processes; the function $\epsilon + \frac{\mu_1 g}{\mu_2 + V}$ in Eq. (4) determines the slow, recovery

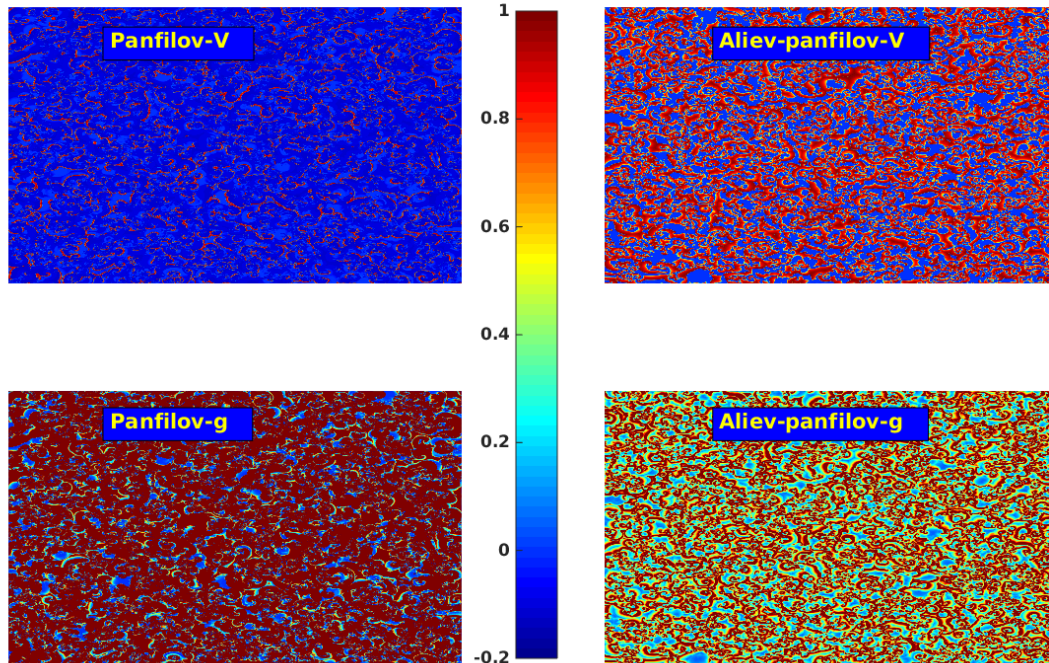


FIG. 3: Pseudocolor plots of the transmembrane potential V (top panels) and the recovery variable g (bottom panels) showing typical turbulent states in our simulations of the 2D Panfilov (left panels) and the Aliev-Panfilov (right panels) models at a representative time, 7.5 (dimensionless units), in the turbulent, statistically steady state, which is, to a good approximation, homogeneous and isotropic far away from boundaries. The spiral-wave initial conditions of Fig. 2 have evolved into small, broken spirals that interact with each other. For the complete spatio temporal evolution of the spirals, see the videos S1,S2,S3 and S4 in the Supplementary Material at [42].

phase of the action potential. For a cell at the location i, j, k in the simulation domain, the total external current I_{ex} is

$$I_{ex} = G[(V_{i+1,j,k} - V_{i,j,k}) + (V_{i-1,j,k} - V_{i,j,k}) + (V_{i,j+1,k} - V_{i,j,k}) + (V_{i,j-1,k} - V_{i,j,k}) + (V_{i,j,k+1} - V_{i,j,k}) + (V_{i,j,k-1} - V_{i,j,k})]. \quad (5)$$

The parameter values we use are ([14]); $\mu_1 = 0.11$, $\mu_2 = 0.3$, $k = 8$, $\epsilon = 0.01$, $a = 0.1$, $b = 0.1$, and $G = 2.772$. To solve the ordinary differential equations in the Aliev-Panfilov model we use the forward-Euler-central-difference scheme. The action potential (AP) for the Aliev-Panfilov model is shown in Fig. 1(b). The action potential duration (APD) for the Aliev-Panfilov model is 42.12 time units (time step of 0.06).

For two-dimensional (2D) simulations we use a 4096×4096 square domain and for three-dimensional (3D) simulations we use a $640 \times 640 \times 640$ cube with the conventional Neumann conditions on the boundaries of our simulation domains. To carry out simulations in such large domains we use Graphics Processing Units (GPUs). We program these GPUs by using CUDA (Compute Unified Device

Architecture) [17]. We use the NVIDIA GPU K20C, with 4 compute nodes, for which we have developed optimized codes for the solutions of the equations for the Panfilov and the Aliev-Panfilov models; these codes are 4 – 5 times faster than their counterparts on a desktop computer with an Intel core-i7-4770, 3.4 GHz system.

We have conducted a detailed statistical analysis of the spiral- and scroll-wave turbulence states in 2D and 3D, respectively, for the Panfilov and the Aliev-Panfilov models. In addition to pseudocolor or isosurface plots of V and g , which show the spatiotemporal evolution of these fields, we have obtained probability distribution functions (PDFs) of V and g and of their gradients; for these PDFs we average data over our simulation domain and over time, after discarding data from initial times during which transients decay and a statistically steady state is established. The size of the domain, the space step and time step used in our DNSs (δx and δt), the total run-time of the program (τ_{tot}), and the transient time during which data are discarded (τ_{trans}) are given in Table I.

For representative results for pseudocolor and isosur-

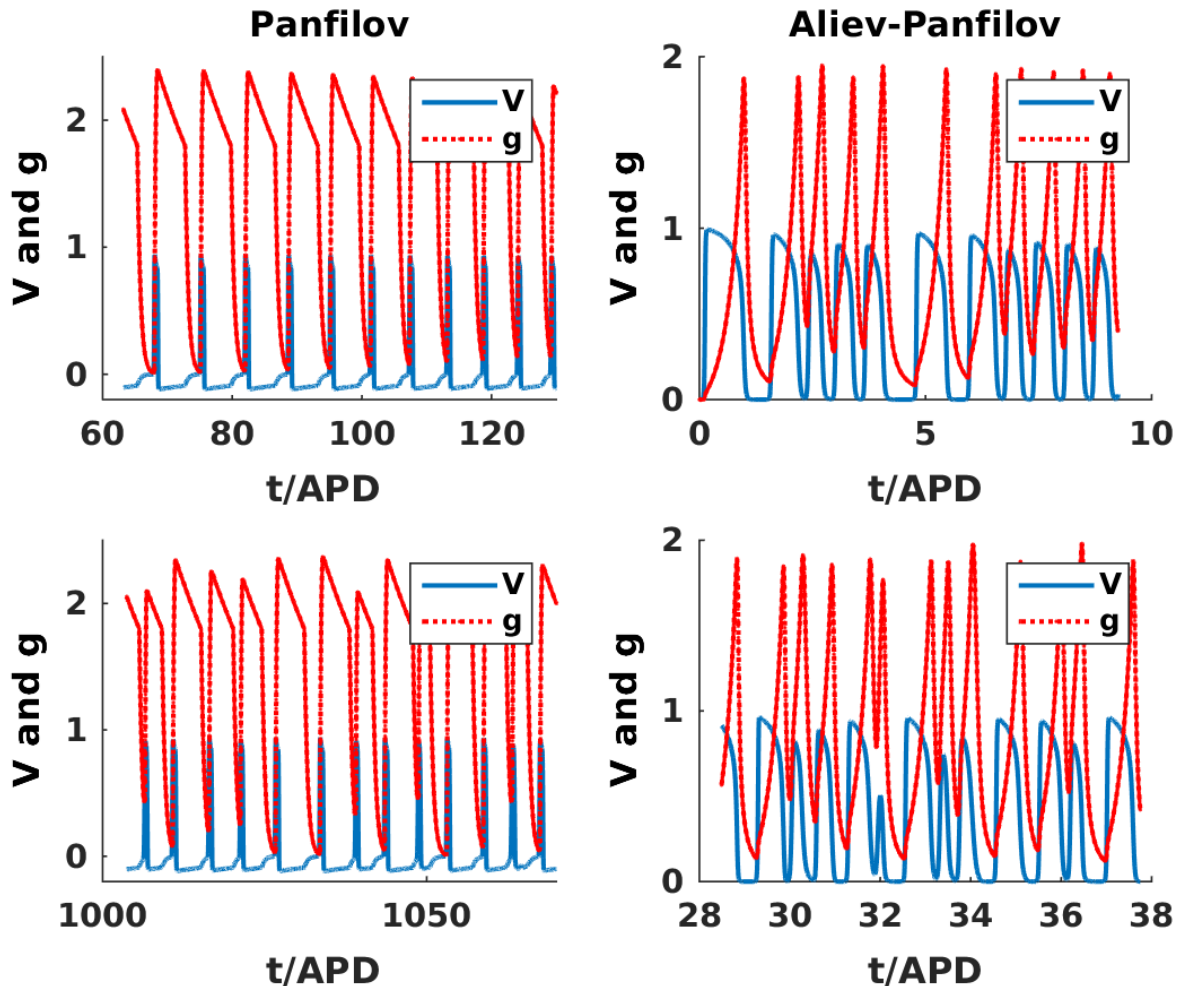


FIG. 4: Plots of the local time series of V (blue lines) and g (red, dashed lines), obtained from the representative point ($x = 2000, y = 2000$) (in dimensionless units), from our 2D domains for the Panfilov (left panels) and the Aliev-Panfilov (right panels) models; time is normalized by the Action Potential Duration (APD), which is 5.92 time units for the Panfilov model and 42.12 time units for the Aliev-Panfilov model (see Fig. 1). The domain size is 4096×4096 . The upper panels show the initial transients in the time series; the lower panels show a section of these time series in the statistically steady, spiral-wave-turbulence states.

face plots for fluid turbulence, in 2D and 3D and for PDFs of the velocity components, the vorticity and velocity gradients, we refer the reader to Refs. [23, 26–28, 30–32]. We note briefly that PDFs of velocity components are very close to Gaussian ones, isosurfaces of the modulus of the vorticity ω show tubes at large values of $|\omega|$ in 3D fluid turbulence, whereas pseudocolor plots of ω in 2D fluid turbulence show, in the absence of friction, the formation of large vortices and antivortices, which are associated with the inverse cascade of energy, from small to large length scales, that we discuss below.

We also calculate the spatial power spectra of V and

g , which are

$$\begin{aligned}
 E_V(k) &= \sum_{k-1/2 \leq k' \leq k+1/2} |\tilde{V}(\mathbf{k}')|^2 \\
 E_g(k) &= \sum_{k-1/2 \leq k' \leq k+1/2} |\tilde{g}(\mathbf{k}')|^2, \quad (6)
 \end{aligned}$$

where the tildes denote spatial Fourier transforms and \mathbf{k} and \mathbf{k}' are wave vectors with magnitudes k and k' , respectively. To eliminate the effects of the boundaries of our simulation domains, we evaluate these Fourier transforms in the central parts of these domains (in 3D we use a region with 512^3 grid points and in 2D a region with 2048^2 grid points).

The fluid-turbulence analogs of these spectra are the energy spectra. We recall that, in 3D fluid turbulence,

TABLE I: The table shows, for each of our DNSs, the size of our simulation domains, the space and time steps δx and δt , respectively, the total run-time of the program (τ_{tot}) and the transient time during which data are discarded (τ_{trans}); numbers are in dimensionless space and time units (see text).

DNS	Domain size	δx	δt	τ_{tot}	τ_{trans}
2D-Panfilov	4096×4096	0.5	0.022	13.2	7
2D-Aliev-Panfilov	4096×4096	0.5	0.06	12	6
3D-Panfilov	$640 \times 640 \times 640$	0.5	0.022	4.62	2.2
3D-Aliev-Panfilov	$640 \times 640 \times 640$	0.5	0.06	6	3

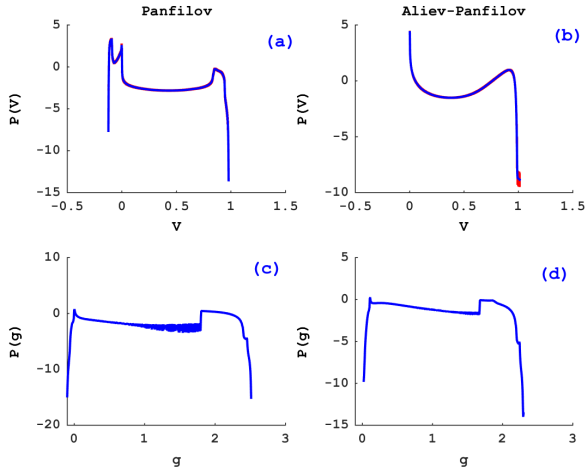


FIG. 5: Plots of PDFs of V for (a) Panfilov and (b) Aliev-Panfilov models and of g for (c) Panfilov and (d) Aliev-Panfilov models in 2D. Here and henceforth, in plots of PDFs, blue curves show the PDF and red symbols the error bars. Error bars are often small and barely visible on the scales of these figures.

the fluid-energy energy spectrum $E(k) \sim k^{-5/3}$ in the inertial range $L^{-1} \ll k \ll \eta_d^{-1}$, where L is the large length at which energy is pumped into the system and η_d the Kolmogorov scale at which viscous dissipation becomes significant [23, 30–32]. This power-law form of the energy spectrum is associated with a forward cascade of energy, à la Richardson, from the energy-injection scale L to the dissipation scale η_d . The spectral exponent $-5/3$ is a consequence of the simple-scaling phenomenology of Kolmogorov [24], which is often denoted by K41; modern experiments and numerical simulations suggest that this exponent is modified slightly because of multiscaling corrections that arise from intermittency [23, 29–31]. Two-dimensional fluid turbulence is qualitatively different from its 3D counterpart [23, 26, 30, 32], as emphasized by Kraichnan [32–36], because the 2D Navier-Stokes equations also conserve the vorticity (the curl of the fluid velocity) in the inviscid, unforced limit. A major consequence of this is that the energy spectrum of homogeneous, isotropic fluid turbulence shows an inverse cas-

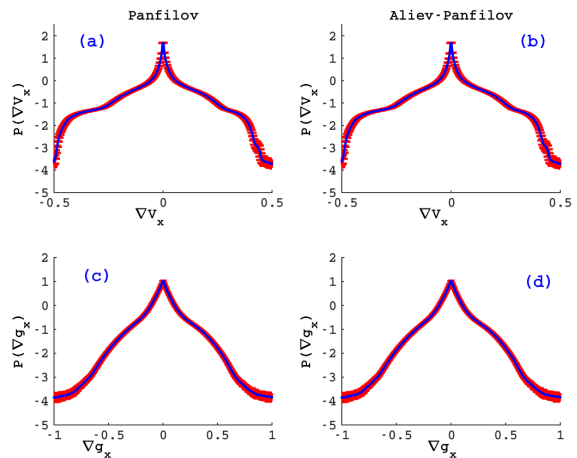


FIG. 6: Semilogarithmic plots (base 10) of PDFs of $(\nabla V)_x$ for (a) Panfilov and (b) Aliev-Panfilov models and similar plots of PDFs of $(\nabla g)_x$ for (c) Panfilov and (d) Aliev-Panfilov models in 2D. These plots show the components of these gradients are highly peaked at zero. PDFs of $(\nabla V)_y$ and $(\nabla g)_y$ show similar plots for the Panfilov and the Aliev-Panfilov models.

cade of energy, from the energy-injection length scale to even larger length scales and a forward cascade of enstrophy (the mean square vorticity) from the energy-injection scale to small length scales. The inverse cascade leads to a scaling region in the energy spectrum $E(k) \sim k^{-5/3}$, whereas the forward cascade yields $E(k) \sim k^{-3}$ (in the absence of any friction on the 2D fluid). In studies of fluid turbulence, the energy spectrum $E(k)$ is used to define the integral length scale

$$L_I = \frac{\int (E(k)/k) dk}{\int E(k) dk} \quad (7)$$

and the Taylor-microscale length

$$L_\lambda = \left[\frac{\int E(k) dk}{\int k^2 E(k) dk} \right]^{1/2}. \quad (8)$$

We calculate the analogs of these lengths for our cardiac-tissue models by using the spectra $E_v(k)$ and $E_g(k)$.

Studies of the statistical properties of fluid turbulence also use order- p structure functions of velocity incre-

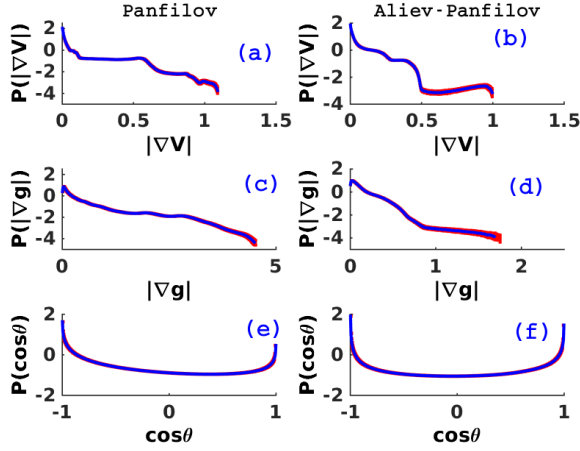


FIG. 7: Semilogarithmic (base 10) plots of the PDFs of (a) $|\nabla V|$, (c) $|\nabla g|$, and (e) $\cos\theta = \frac{\nabla V \cdot \nabla g}{|\nabla V||\nabla g|}$ for the 2D Panfilov model; (b), (d), and (f) show, respectively, the corresponding PDFs for the 2D Aliev-Panfilov model. $|\nabla V|$ and $|\nabla g|$ show dominant peaks at zero. Figures (e) and (f) show that V and g either tend to align or antialign with each other; the tendency for being antialigned ($\cos\theta = -1$) is stronger than the tendency for alignment ($\cos\theta = 1$).

ments [23, 30]; therefore, we calculate their counterparts for V and g . We illustrate this for structure functions of V . We follow Ref. [37, 38] and calculate $V'(\mathbf{r}) = V - \langle V \rangle_t$, where $\langle \rangle_t$ denotes an average over time; we define

$$S_p(r) = \langle \{ [V'(\mathbf{r}_c + \mathbf{r}, t) - V'(\mathbf{r}_c, t)] \cdot \mathbf{r}/r \}^p \rangle_{\mathbf{r}_c}, \quad (9)$$

where \mathbf{r} has magnitude r and \mathbf{r}_c is an origin and $\langle \rangle_{\mathbf{r}_c}$ denotes an average over time and the origin. The fluid-turbulence analogs of $S_p(r)$ scale as r^{ζ_p} for $\eta_d \ll r \ll L$. The K41 result is $\zeta_p = \zeta_p^{K41} = p/3$; experimental and numerical studies show that simple scaling is replaced by multiscaling, i.e., the multiscaling exponents ζ_p deviate significantly from ζ_p^{K41} , especially for $p > 3$. The multiscaling exponents ζ_p can be determined from the slopes of linear regions in log-log plots of $S_p(r)$ versus r . In any finite-resolution study, such as a DNS, this linear region is limited, so an accurate determination of ζ_p is a challenge, particularly for large values of p . The range over which such exponents can be fit can be enlarged by using the extended-self-similarity (ESS) procedure [39, 40] in which slopes of linear regions in log-log plots of $S_p(r)$ versus $S_3(r)$ yield the exponent ratios ζ_p/ζ_3 . (In the fluid-turbulence context, $\zeta_3 = 1$, by virtue of the von Kármán-Howarth relation [32], so a determination of ζ_p/ζ_3 yields ζ_p .) We use this ESS procedure to look for signatures of multiscaling the order- p structure functions of V . Numerical studies of 2D fluid turbulence suggest the velocity analogs of Eq. 9 do not exhibit multiscaling, but the vorticity always do [29, 37, 38].

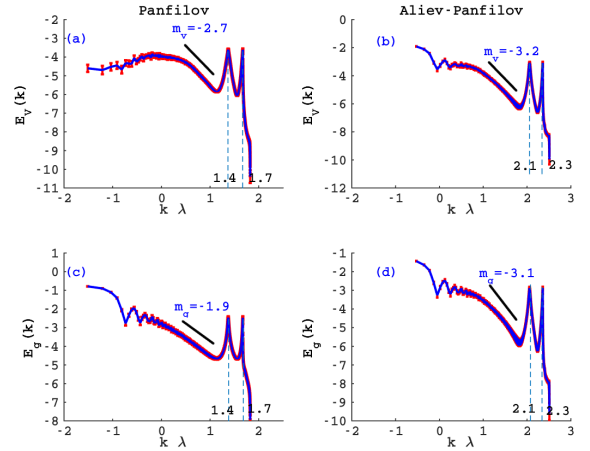


FIG. 8: Log-log (base 10) plots of the spectra $E_V(k)$ and $E_g(k)$ versus $k\lambda$; here $\lambda = 10$ dimensionless units for the Panfilov model and $\lambda = 48.5$ dimensionless units for the Aliev-Panfilov model, represents the wavelength of a plane wave in the medium. The dashed, black line shows a possible power-law regime. The overall shapes of these spectra are similar in both models; in particular, we see two prominent peaks in these spectra, located at $k\lambda = 1.4$ and $k\lambda = 1.7$ (Panfilov model) and at $k\lambda = 2.1$ and $k\lambda = 2.4$ (Aliev-Panfilov model).

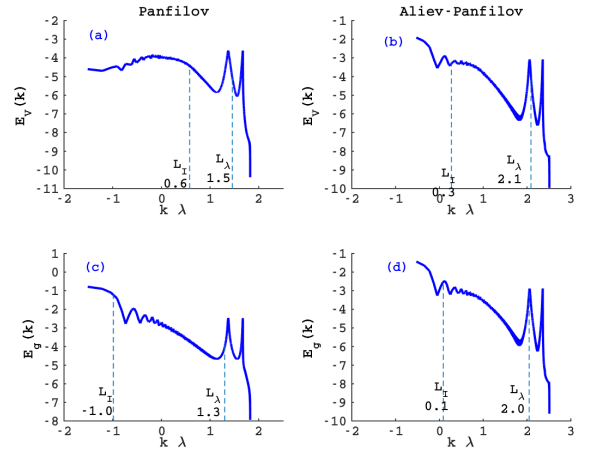


FIG. 9: Log-log (base 10) plots of the spectra $E_V(k)$ and $E_g(k)$ versus $k\lambda$, with the positions of the Taylor micro length scale, L_λ and the Integral length scale, L_I .

III. RESULTS

In this Section, we first present results from our simulations for spiral-wave turbulence for the 2D Panfilov and the Aliev-Panfilov models. We then give results from our studies of scroll-wave turbulence for these two models in 3D.

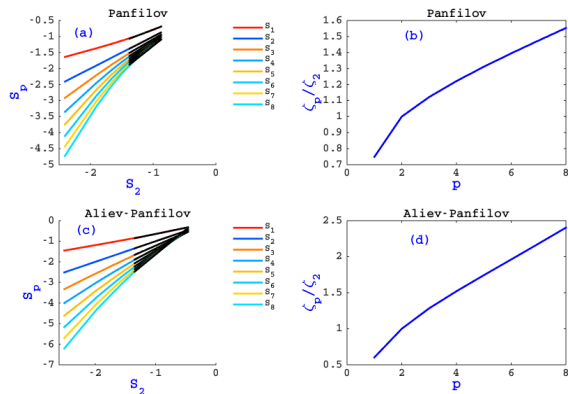


FIG. 10: Extended-self-similarity (ESS) plots of the structure functions S_p of V versus S_2 for 2D (a) Panfilov and (c) Aliev-Panfilov models, with $1 \leq p \leq 8$; the dashed (-) black lines represent possible power-law regimes. In (b) and (d), we show plots versus p of the exponent ratios $\frac{C_p}{C_2}$ for the two models. The curvature of the plot of $\frac{C_p}{C_2}$ versus p indicates multiscaling.

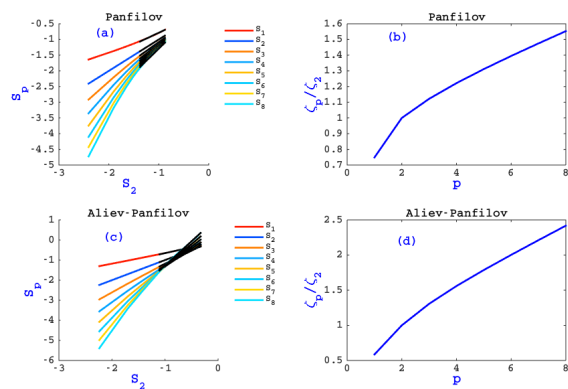


FIG. 11: Extended-self-similarity (ESS) plots of the structure functions S_p of g versus S_2 for 2D (a) Panfilov and (c) Aliev-Panfilov models, with $1 \leq p \leq 8$; the dashed (-) black lines represent possible power-law regimes. In (b) and (d), we show plots versus p of the exponent ratios $\frac{C_p}{C_2}$ for the two models. The curvature of the plot of $\frac{C_p}{C_2}$ versus p indicates multiscaling.

A. Results for two-dimensional spiral-wave turbulence

Our DNSs in 2D use a domain of size 4096×4096 . We begin with half the medium excited and the other half in the excitable state; and then we apply a stimulus at the middle of the domain to form a spiral wave, which we use as an initial condition. Figure 2 shows pseudocolor plots of the transmembrane potential V (top panels) and the recovery variable g (bottom panels) with the spiral waves that we use as initial conditions for our simulations

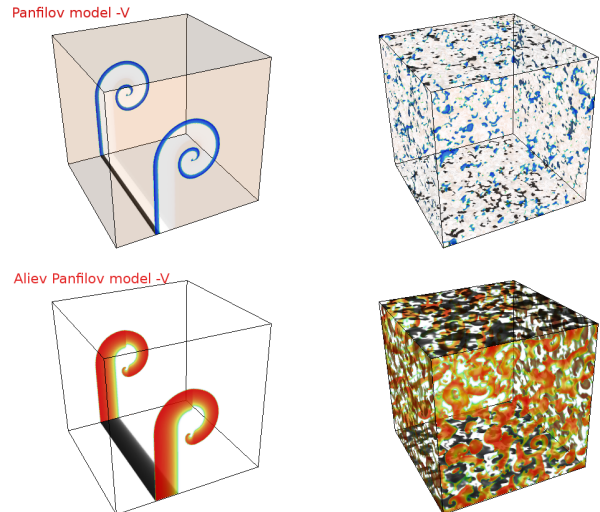


FIG. 12: Pseudocolor plots of the transmembrane potential V showing the scroll waves that we use as initial conditions for our simulations of the 3D Panfilov (top, left panel) and the Aliev-Panfilov (bottom, left panel) models and typical turbulent states in our simulations of the 3D Panfilov (top, right panel) and Aliev-Panfilov (bottom, right panel) models, at a representative time, $t = 3.8$ (dimensionless units), in the turbulent, statistically steady state, which is, to a good approximation, homogeneous and isotropic far away from boundaries. For the complete spatio temporal evolution of the scrolls, see movies S5 and S6 in the Supplementary Material at [42].

of the 2D Panfilov (left panels) and the Aliev-Panfilov (right panels) models. Given our set of parameter values, these spiral waves break up and the medium is filled with broken spiral waves. Figure 3 shows pseudocolor plots of the transmembrane potential V (top panels) and the recovery variable g (bottom panels) that depict typical turbulent states in our simulations of the 2D Panfilov (left panels) and the Aliev-Panfilov (right panels) models at a representative time, 7.5 (dimensionless units), in the turbulent, statistically steady state, which is, to a good approximation, homogeneous and isotropic far away from boundaries. Note that the spiral-wave initial conditions of Fig. 2 evolve into small, broken spirals that interact with each other. This is the analog of the Richardson cascade in fluid turbulence. Instead of large eddies breaking down into ever smaller and lighter eddies, here a large spiral wave breaks down into smaller and smaller spiral waves. These pseudocolor plots can be contrasted with their analogs for the vorticity in 2D fluid turbulence [37], where the typical sizes of vortical regions are governed by (a) the energy-injection length scale and (b) whether or not there is air-drag-induced friction on the 2D fluid.

After the system reaches a statistically steady state, we record the values of V and g ; and we then calculate their statistical properties, which we describe below.

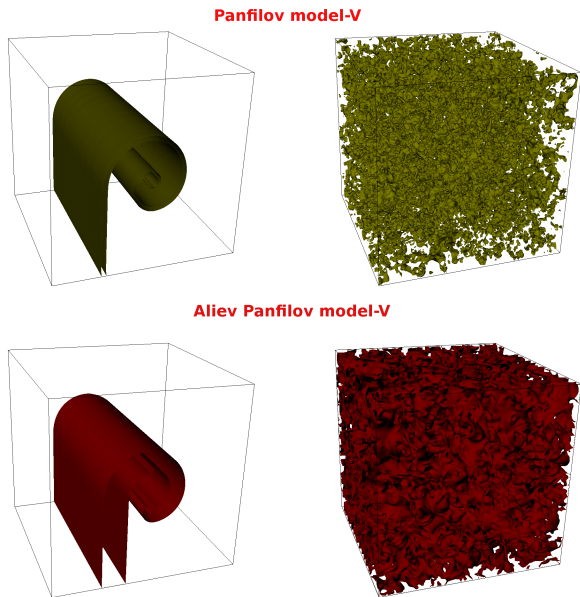


FIG. 13: Isosurface plots, for the 3D Panfilov (top panels) and Aliev-Panfilov (bottom panels) models, of the transmembrane potential V (isosurfaces with $V = 0.8$), showing the scroll waves that we use as initial conditions for our simulations of the 3D Panfilov (top, left panel) and the Aliev-Panfilov (bottom, left panel) models and typical turbulent states in our simulations of the 3D Panfilov (top, right panel) and Aliev-Panfilov (bottom, right panel) models, at a representative time, 3.8 (dimensionless units), in the turbulent, statistically steady state, which is, to a good approximation, homogeneous and isotropic far away from boundaries. For the complete spatio-temporal evolution of the scrolls, see movies S7 and S8 in the Supplementary Material at [42].

B. Statistical properties of spiral-wave turbulence

Figure 1 shows typical action potentials for the Panfilov (top panel) and the Aliev-Panfilov (bottom panel) models, illustrating the depolarization, plateau, repolarization, and resting states of the excitable medium. We present our results in Figs. 4-11. Figure 4 shows local time series of V (blue lines) and g (red dashed lines), obtained from the representative point ($x = 2000, y = 2000$) (in dimensionless units) from our 2D domains for the Panfilov (left panels) and the Aliev-Panfilov (right panels) models; time is normalized by the action-potential duration (APD), which is 5.92 time units for the Panfilov model and 42.12 time units for the Aliev-Panfilov model. The upper panels show the initial transients in the time series; the lower panels show a section of these time series in the statistically steady, spiral-wave-turbulence states. The time series of V consists of a train of action potentials. Note that the action potential for the Aliev-Panfilov model does not have an overshoot region (Fig. 1(b)), where the system repolarizes beyond its resting state.

Figure 5 contains plots of PDFs of V for (a) Panfilov and (b) Aliev-Panfilov models and of g for (c) Panfilov and (d) Aliev-Panfilov models in 2D. Here and henceforth, in plots of PDFs, blue curves show PDFs and red symbols the error bars. The PDF of V for the Panfilov model shows two peaks in the small- V region. One peak corresponds to the overshoot region in the time series and the other peak corresponds to the resting state. The peak at high values of V (or g) corresponds to the excited and the plateau regions. These PDFs for the Aliev-Panfilov model have only one peak, in the small- V region, at zero. This is because the Aliev-Panfilov model does not have an overshoot region in its action potential; one peak in the PDF of V corresponds to the resting state and the other peak, at a high value, corresponds to the excited state and the plateau states. Error bars are small and are barely visible on the scales of these figures. Note that these PDFs depend on the details of these models; and they are markedly different from the approximately Gaussian PDFs of velocity components in fluid turbulence [30].

Figure 6 contains semilogarithmic (base 10) plots of PDFs of $(\nabla V)_x$ for (a) Panfilov and (b) Aliev-Panfilov models in 2D and PDFs of $(\nabla g)_x$ for (c) Panfilov and (d) Aliev-Panfilov models in 2D. Figure 6 shows that the PDFs of ∇V_x exhibit sharp peaks at zero; the PDFs of ∇g_x have sharp peaks at zero, like those in the PDFs of ∇V_x ; the PDFs of $(\nabla V)_y$ and $(\nabla g)_y$ for the Panfilov and the Aliev-Panfilov models are similar. These gradient PDFs are sharply peaked at zero, indicating that, on average, these gradients are small; however, these gradients have flat, non-Gaussian tails and, in this regard, are qualitatively similar to the non-Gaussian tails of PDFs of velocity gradients in fluid turbulence.

Figure 7 contains semilogarithmic (base 10) plots of the PDFs of (a) $|\nabla V|$, (c) $|\nabla g|$ and (e) $\cos \theta = \frac{\nabla V \cdot \nabla g}{|\nabla V| |\nabla g|}$ for the 2D Panfilov model; Figures 7 (b), (d) and (f) show, respectively, the corresponding PDFs for the 2D Aliev-Panfilov model. For both these models, the PDFs of $|\nabla V|$ and $|\nabla g|$ show dominant peaks at zero. Figures 7 (e) and (f) show that, on average, ∇V and ∇g tend either to align or to antialign with each other; the tendency for being antialigned ($\cos \theta = -1$) is stronger than the tendency for alignment ($\cos \theta = 1$). For cardiac models this may be a consequence of the recovery processes (described by g) normally building up when the excitation (variable V) has already decayed (see Fig. 4). The nearest analogs of these in fluid turbulence are PDFs of the angles between the velocity and the vorticity in 3D fluid turbulence (see, e.g., Fig. 2d in Ref. [28]).

Figure 8 contains log-log (base 10) plots of the spectra $E_V(k)$ and $E_g(k)$ versus $k\lambda$; here $\lambda = 10$, in dimensionless units for the Panfilov model, and $\lambda = 48.5$, in dimensionless units for the Aliev-Panfilov model, represents the wavelength of a plane wave in the medium. The dashed, black lines show (possible) power-law regime, with $E_v(k) \sim k^{m_v}$ and $E_g(k) \sim k^{m_g}$ and $m_v \simeq -2.7$ (Panfilov), $m_v \simeq -3.2$ (Aliev-Panfilov), $m_g \simeq -1.9$

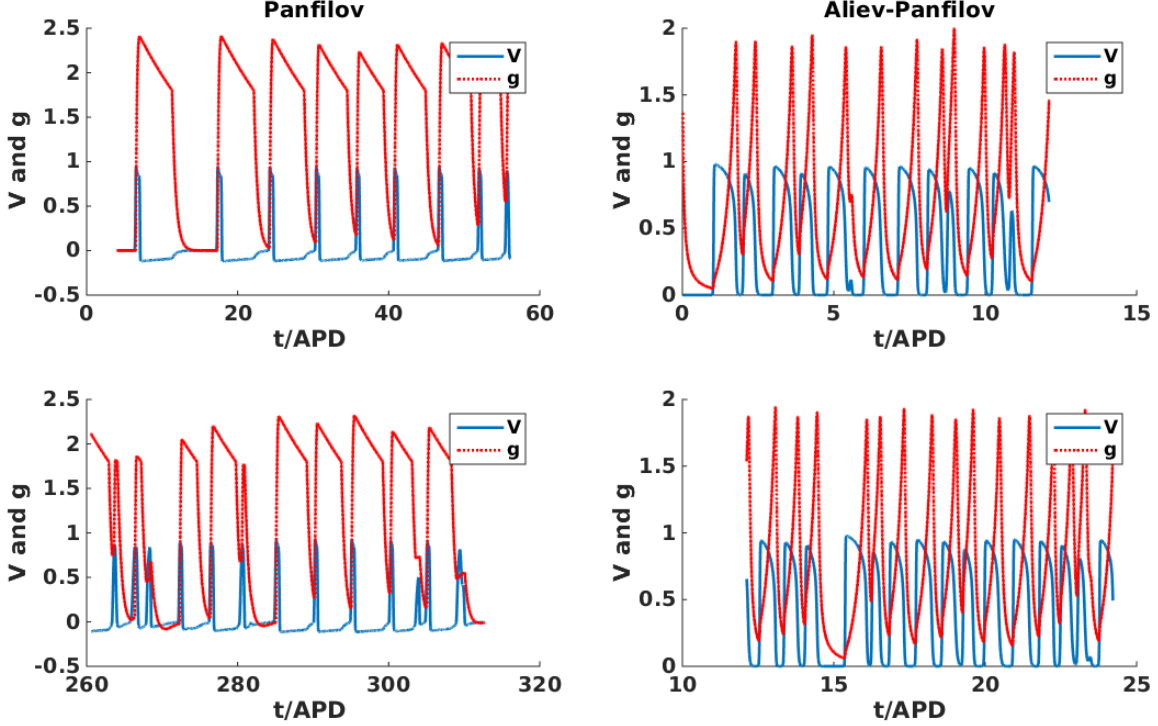


FIG. 14: Local time series of V (blue lines) and g (red dashed lines), obtained from the representative point ($x = 200, y = 200, z = 300$) (in dimensionless units) from our 3D domains for the Panfilov (left panels) and the Aliev-Panfilov (right panels) models; time is normalized with the action-potential duration (APD); APD= 5.92 time units for the Panfilov model; APD= 42.12 time units for the Aliev-Panfilov model. The domains size is $640 \times 640 \times 640$. The upper panels show the initial transients in the time series; the lower panels show a section of these time series in the statistically steady, scroll-wave-turbulence states. The time series of V consists of a train of action potentials showing the states of depolarization, plateau state, repolarization, and resting state of the excitable medium. The action potential for the Aliev-Panfilov model does not have an overshoot region, where the system repolarizes beyond its resting state.

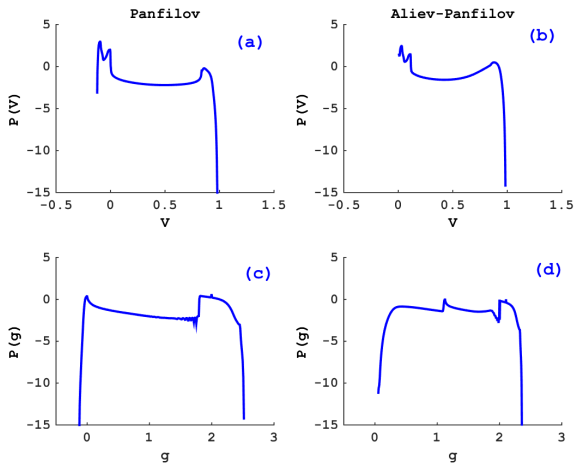


FIG. 15: Probability distribution functions (PDFs) of V for (a) Panfilov and (b) Aliev-Panfilov models and of g for (c) Panfilov and (d) Aliev-Panfilov models in 3D.

(Panfilov), $m_g \simeq -3.1$ (Aliev-Panfilov). The shapes of these spectra are qualitatively similar in both models. In particular, we see two prominent peaks in these spectra, located at $k\lambda = 1.4$ and $k\lambda = 1.7$ (Panfilov model) and at $k\lambda = 2.1$ and $k\lambda = 2.4$ (Aliev-Panfilov model). However, these power-law regimes are certainly not as universal as their fluid-turbulence counterparts in $E(k)$; nevertheless, the spectral slopes, -2.7 and -3.2 for $E_V(k)$ are reasonably close to each other; thus, the issue of their universality requires detailed, high-resolution studies in other models and conditions. If these spectral exponents are not universal, we conjecture that this is because of the large number of parameters in the models we consider; in particular, this means that we cannot develop, in any obvious way, the spiral-turbulence analog of the K41 phenomenological theory for the scaling of fluid-turbulence, inertial-range energy spectra.

We have calculated the integral length scale L_I and the Taylor-micro length L_λ by using the spectrum $E_V(k)$. They are 2.62 and 0.35, respectively, for the 2D Panfilov model and 25.88 and 0.39, respectively, for the 2D Aliev-

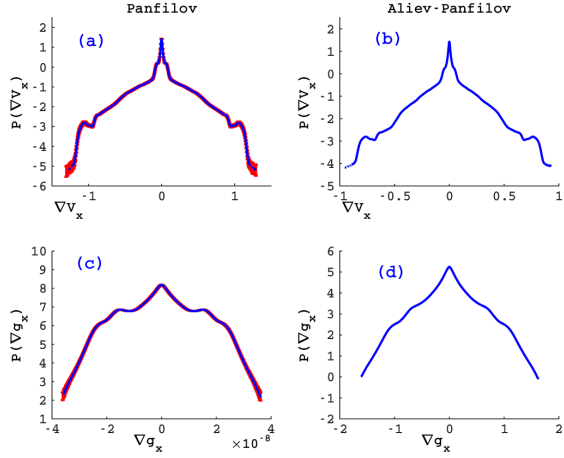


FIG. 16: Semilogarithmic (base-10) plots of PDFs of $(\nabla V)_x$ for (a) Panfilov and (b) Aliev-Panfilov models and $(\nabla g)_x$ for (c) Panfilov and (d) Aliev-Panfilov models in 3D. These plots show dominant peaks at zero. The PDFs of $(\nabla V)_y$ and of $(\nabla V)_z$ are like those of $(\nabla V)_x$; and PDFs of $(\nabla g)_y$ and of $(\nabla g)_z$ are akin to those of $(\nabla g)_x$.

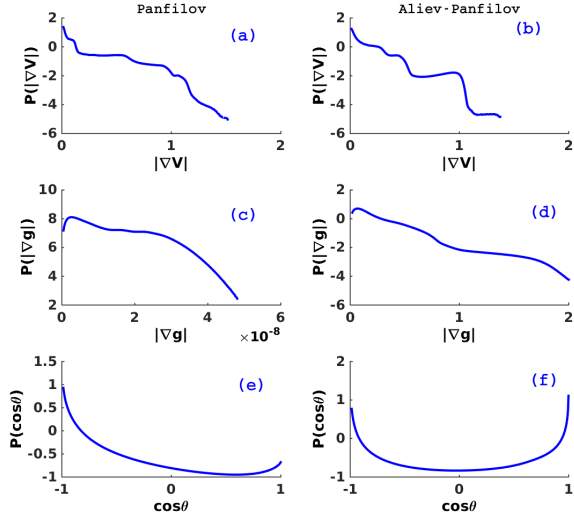


FIG. 17: Semilogarithmic (base 10) plots of the PDFs of (a) $|\nabla V|$, (c) $|\nabla g|$ and (e) $\cos\theta = \frac{\nabla V \cdot \nabla g}{|\nabla V||\nabla g|}$ for the 3D Panfilov model; (b), (d) and (f) show, respectively, the corresponding PDFs for the 3D Aliev-Panfilov model; PDFs in (e) and (f) show that ∇V and ∇g tend, on average, either to align or anti-align with each other. The degree of alignment or anti-alignment is different in these two models; for the Panfilov model, the tendency for being antialigned ($\cos\theta = -1$) is stronger than the tendency for alignment ($\cos\theta = 1$).

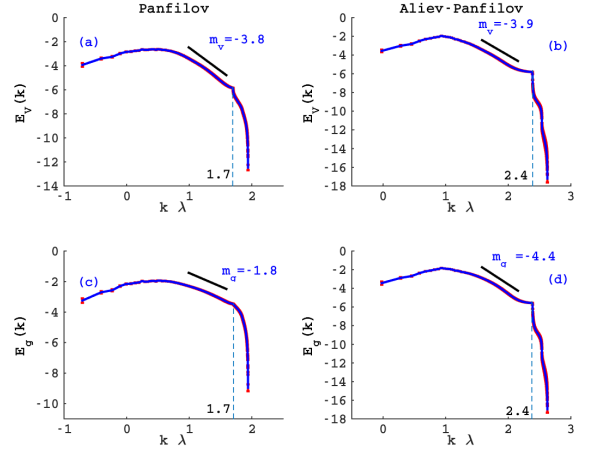


FIG. 18: Log-log (base 10) plots of the spectra $E_V(k)$ and $E_g(k)$ versus $k\lambda$. Here $\lambda = 10$, in dimensionless units for the Panfilov model, and $\lambda = 48.5$, in dimensionless units for the Aliev-Panfilov model, represents the wavelength of a plane wave in the medium. The dashed, black lines show (possible) power-law regimes. The overall shapes of these spectra are similar in both models. We see one prominent peak in these spectra. This peak is located at $k\lambda = 1.7$ (Panfilov model) and $k\lambda = 2.4$ (Aliev-Panfilov model).

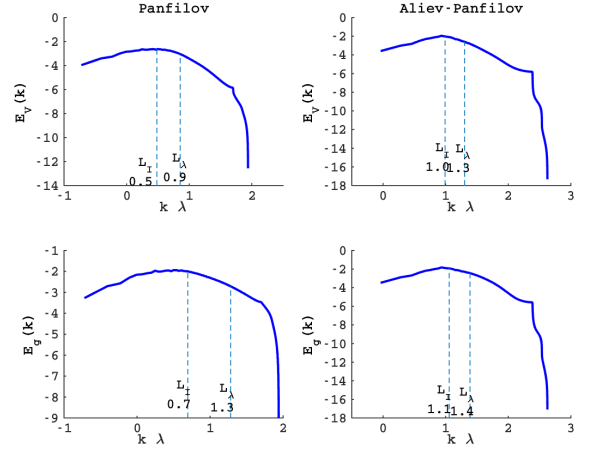


FIG. 19: Log-log (base 10) plots of the spectra $E_V(k)$ and $E_g(k)$ versus $k\lambda$, with the positions of the Taylor micro length scale, L_λ and the Integral length scale, L_I .

Panfilov model. By using the spectrum $E_g(k)$, we find L_I and L_λ to be 97.03 and 0.50, respectively, for the Panfilov model and 39.63 and 0.43, respectively, for the Aliev-Panfilov model. The inversus of these lengthscales are shown, by dashed lines, in the spectra given in Fig. 9.

In studies of fluid turbulence, it has been found that the power-law regime in $S_p(r)$ can be *extended* by using the *extended self similarity* (ESS) procedure, in which we

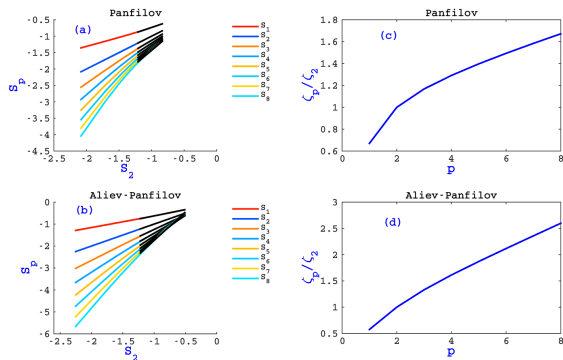


FIG. 20: Extended-self-similarity (ESS) plots of the structure functions S_p of V versus S_2 for 3D Panfilov (top, left panel) and Aliev-Panfilov (bottom, left panel) models, with $1 \leq p \leq 8$; the dashed-black lines indicate (possible) power-law regimes. In (b) and (d), we show plots of the exponent ratios ζ_p/ζ_2 versus p for the two models. The curvature of ζ_p/ζ_2 versus p indicates multiscaling.

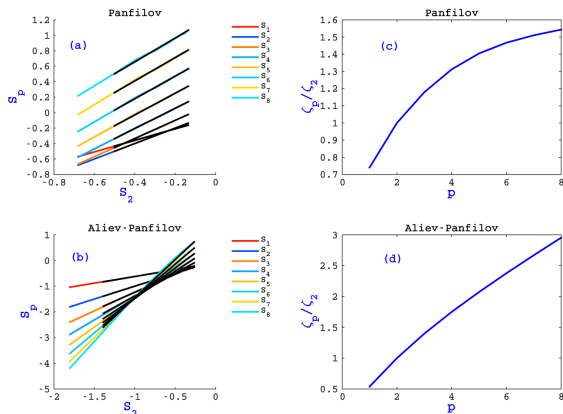


FIG. 21: Extended-self-similarity (ESS) plots of the structure functions S_p of g versus S_2 for 3D Panfilov (top, left panel) and Aliev-Panfilov (bottom, left panel) models, with $1 \leq p \leq 8$; the dashed-black lines indicate (possible) power-law regime. In (b) and (d), we show plots of the exponent ratios ζ_p/ζ_2 versus p for the two models. The curvature of ζ_p/ζ_2 versus p indicates multiscaling.

plot $S_p(r)$ versus some other structure function $S_{p1}(r)$. In Fig. 10 we give such log-log (base 10) extended-self-similarity (ESS) plots of $S_p(r)$ versus $S_2(r)$ of V for 2D (a) Panfilov and (c) Aliev-Panfilov models with $1 \leq p \leq 8$; the dashed-black lines represent (possible) power-law regime. The power-law ranges in these plots yield the multiscaling exponent ratios ζ_p/ζ_2 , which we plot versus p in Fig. 10 (b) and (d). In Fig. 11 we give such log-log (base 10) extended-self-similarity (ESS) plots of $S_p(r)$ versus $S_2(r)$ of g for 2D (a) Panfilov and (c) Aliev-Panfilov models with $1 \leq p \leq 8$; the dashed-

black lines represent (possible) power-low regimes. The power-law ranges in these plots yield the multiscaling exponent ratios ζ_p/ζ_2 , which we plot versus p in Fig. 11 (b) and (d). These exponent ratios should be viewed with great caution, for they contain ratios of small numbers; this becomes apparent if we plot structure functions versus r and do not use the ESS procedure. Whether or not such structure functions display multiscaling can be settled only by DNSs that use much larger domains and longer runs than those we have been able to perform. As we have mentioned in the context of spectral exponents, the exponents or exponent ratios for the Panfilov and Aliev-Panfilov models are comparable to each other, but not equal at the resolution of our DNSs; the issue of their universality or lack thereof requires detailed, high-resolution studies in other models and conditions.

C. Three-dimensional results for scroll-wave turbulence

Our DNSs in 3D use a domain of size $640 \times 640 \times 640$. We begin with half the medium excited and the other half in the excitable state; and then we apply a stimulus at the middle of the domain to form a scroll wave, which we use as an initial condition (Fig. 13). Figure 12 presents pseudocolor plots of the transmembrane potential V showing the scroll waves we use as initial conditions for our simulations of the 3D Panfilov (top, left panel) and the Aliev-Panfilov (bottom, left panel) models, and typical turbulent states in our simulations of the 3D Panfilov (top, right panel) and Aliev-Panfilov (bottom, right panel) models, at a representative time, 3.8 (dimensionless units), in the turbulent, statistically steady state, which is, to a good approximation, homogeneous and isotropic far away from boundaries. Given our set of parameter values, the scroll-wave initial conditions have evolved into small, broken scrolls that interact with each other. After the system has reached a statistically steady state, we record the values of V and g and calculate the statistical properties of this state. We present our results in Figs. 14-21.

In Fig. 13 we portray the initial and final states of our 3D system for the two models by using isosurface plots of V for $V = 0.8$ (dimensionless units). Note that the scroll-wave initial conditions have evolved into small, broken scrolls that interact with each other. This is the analog of the Richardson cascade in fluid turbulence. Instead of large eddies breaking down into ever smaller eddies, here a large scroll wave breaks down into smaller and smaller scroll waves. These isosurfaces of V should be contrasted with the tubular structures of isosurfaces of the modulus of the vorticity in 3D fluid turbulence [27, 28, 30].

Figure 14 shows local time series of V (blue lines) and g (red dashed lines), obtained from the representative point ($x = 200, y = 200, z = 300$) (in dimensionless units) from our 3D domains for the Panfilov (left panels) and the Aliev-Panfilov (right panels) models; time is normalized

by the action-potential duration (APD), which is 5.92 time units, for the Panfilov model, and 42.12 time units, for the Aliev-Panfilov model. The upper panels show the initial transients in these time series; the lower panels show a section of these time series in the statistically steady, scroll-wave-turbulence states. The time series of V consists of a train of action potentials. The action potential for the Aliev-Panfilov model does not have an overshoot region (see Fig. 1), where the system repolarizes beyond its resting state.

Figure 15 contains plots of PDFs of V for (a) Panfilov and (b) Aliev-Panfilov models and of g for (c) Panfilov and (d) Aliev-Panfilov models in 3D. As in our 2D simulation, the PDF of V , for the Panfilov model in 3D, shows two peaks in the small- V region. One peak corresponds to the overshoot region in the APD and the other corresponds to the resting state. The peak at a high value of V (or g) corresponds to the excited and the plateau region. These PDFs for the Aliev-Panfilov model have a peak in the small- V region at $V = 0$. The Aliev-Panfilov model does not have an overshoot region in its action potential. Its one peak corresponds to the resting state and the other peak, at a high value of V , corresponds to the excited and the plateau states.

Figure 16 contains semilogarithmic (base-10) plots of PDFs of $(\nabla V)_x$ for (a) Panfilov and (b) Aliev-Panfilov models in 3D. These figures show dominant peaks at zero. The PDFs of $(\nabla V)_y$ and of $(\nabla V)_z$ are similar. In Fig. 16 the bottom panels contain semilogarithmic (base 10) plots of PDFs of $(\nabla g)_x$ for (c) Panfilov and (d) Aliev-Panfilov models in 3D. The dominant peaks are at zero. The PDFs of $(\nabla g)_y$ and $(\nabla g)_z$ are similar.

Figure 17 contains plots of the PDFs of (a) $|\nabla V|$, (c) $|\nabla g|$, and (e) $\cos \theta = \frac{\nabla V \cdot \nabla g}{|\nabla V| |\nabla g|}$ for the 3D Panfilov model; (b), (d), and (f) show, respectively, the corresponding PDFs for the 3D Aliev-Panfilov model. For both these models, the PDFs of $|\nabla V|$ and $|\nabla g|$ show dominant peaks at zero. Figures 17 (e) and (f) show that, on average, ∇V and ∇g tend either to align or to anti-align with each other. The degree of alignment or anti-alignment is different in these two models; for the Panfilov model, the tendency for being anti-aligned ($\cos \theta = -1$) is stronger than the tendency for alignment ($\cos \theta = 1$).

Figure 18 contains log-log (base 10) plots of the spectra $E_V(k)$ and $E_g(k)$ versus $k\lambda$; here $\lambda = 10$, in dimensionless units for the Panfilov model, and $\lambda = 48.5$, in dimensionless units for the Aliev-Panfilov model. The dashed, black line shows a (possible) power-law regimes, with $E_v(k) \sim k^{m_v}$ and $E_g(k) \sim k^{m_g}$ and $m_v \simeq -3.8$ (Panfilov), $m_v \simeq -3.9$ (Aliev-Panfilov), $m_g \simeq -1.8$ (Panfilov), and $m_g \simeq -4.4$ (Aliev-Panfilov). The shapes of these spectra are qualitatively similar in both models; in particular, we see one sharp feature in these spectra, located at $k\lambda = 1.7$ (Panfilov model) and at $k\lambda = 2.4$ (Aliev-Panfilov model). The spectral slopes, -3.8 and -3.9 , for $E_V(k)$ are reasonably close to each other; but, as we have noted in our discussion of our 2D-spiral-wave-

turbulence results, the issue of the universality of these exponents requires detailed, high-resolution studies in other models and conditions.

We have calculated the integral length scale L_I and the Taylor-micro length L_λ by using the spectrum $E_V(k)$. They are 3.28 and 1.39, respectively, for the 3D Panfilov model and 4.95 and 2.41, respectively, for the 3D Aliev-Panfilov model. By using the spectrum $E_g(k)$, we find L_I and L_λ to be 2.01 and 0.52, respectively, for the Panfilov model and 4.26 and 1.98, respectively, for the Aliev-Panfilov model. The inversus of these lengthscales are shown, by dashed lines, in the spectra given in Fig. 19.

In Fig. 20 we give log-log (base 10) extended-self-similarity (ESS) plots of $S_p(r)$ versus $S_2(r)$ of V for 3D (a) Panfilov and (c) Aliev-Panfilov models with $1 \leq p \leq 8$. The dashed-black lines represent (possible) power-law regimes. The power-law ranges in these plots yield the multiscaling exponent ratios ζ_p/ζ_2 , which we plot versus p in Fig. 20 (b) and (d). In Fig. 21 we give such log-log (base 10) extended-self-similarity (ESS) plots of $S_p(r)$ versus $S_2(r)$ of g for 3D (a) Panfilov and (c) Aliev-Panfilov models with $1 \leq p \leq 8$. The power-law ranges in these plots yield the multiscaling exponent ratios ζ_p/ζ_2 , which we plot versus p in Fig. 21 (b) and (d). Our cautionary remarks, for ESS plots in the case of 2D, spiral-wave turbulence, apply here too.

D. Scroll-wave turbulence with negative filament tension

The breakdown of scroll waves has been studied in a model, for cardiac tissue, that displays negative filament tension [41]. Such studies have not used simulation domains that are large enough to yield statistically homogeneous and isotropic scroll-wave turbulence. Therefore, we have carried out a study of scroll-wave turbulence in a parameter regime in the Aliev-Panfilov model in which the filament tension is negative. In this case, the scroll sheets show undulations in the transverse direction, which indicates that the scroll filament has a negative tension; it first becomes elongated, and then it breaks up; this is shown in Fig. 22. The parameter set for the Aliev-Panfilov model, which gives rise to this behavior of the scroll-waves, is $\mu_1 = 0.05$; $\mu_2 = 0.30$; and $g = g_{min} * 74$, where $g_{min} = 0.033$. We have calculated the spectra E_V and E_g for this case and found that, as far as statistical properties of scroll-wave turbulence are concerned, there is no significant difference between the statistical properties of 3D-scroll-wave turbulence, with and without negative tension for the scroll filament. This interesting universality of scroll-wave turbulence (i.e., spectral exponents that do not seem to depend on the filament tension of the initial scroll wave) is illustrated in the log-log plots of Fig. 23, which compare the spectra E_V and E_g for scroll-wave turbulence with and without negative filament tension. Figure 24 shows a comparison of ESS plots of structure functions for both these cases.

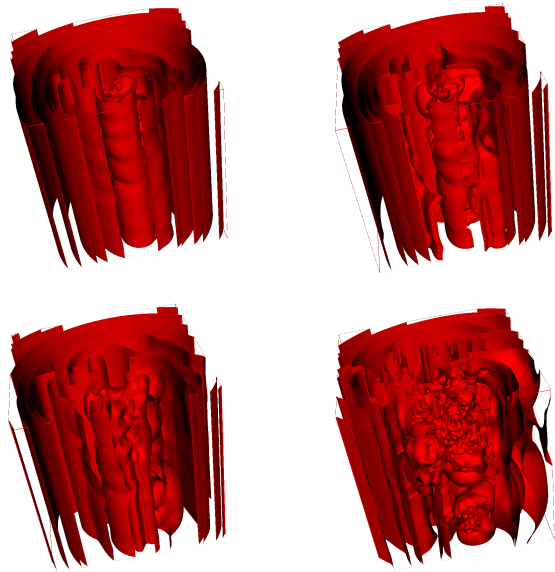


FIG. 22: Isosurface plots of scroll-wave formation and subsequent break up in the case of the Aliev-Panfilov model with parameters such that the scroll filament has a negative tension, which is manifest here in the transverse undulations in the scroll sheets. For the complete spatio temporal evolution of th scrolls, see movie S9 in the Supplementary Material at [42].

IV. CONCLUSION

We have carried out the most extensive numerical study, attempted so far, of the statistical properties of scroll-and spiral- wave turbulence in two simple, two-variable models for cardiac tissue. In particular, we have examined, via extensive direct numerical simulations (DNSs), the statistical properties of spiral- and scroll-wave turbulence in two- and three-dimensional excitable media by using the Panfilov [13] and the Aliev-Panfilov [14] mathematical models for cardiac tissue. We use very large simulation domains, made possible by our state-of-the-art simulations on graphics processing units (GPUs) [17], with a view to comparing the statistical properties of spiral- and scroll-wave turbulence here with the statistical properties of statistically homogeneous and isotropic two- and three-dimensional fluid turbulence. We hope our study of the statistical properties of homogeneous and isotropic spiral- and scroll-wave turbulence will stimulate experimental studies of such turbulence.

As we have noted above, there is an important qualitative difference between spiral- and scroll-wave turbulence in excitable media and fluid turbulence insofar as

turbulence in an excitable medium is neither decaying nor forced. Once turbulence has been initiated in an excitable medium, e.g., by a large spiral or scroll wave, we have shown that there is a forward cascade, which yields small spirals or scrolls; these form, interact, and break all the time. We have shown that the resulting turbulent state is statistically steady and, far away from boundaries, is statistically homogeneous and isotropic. For the fields V and g , we have shown that the spectral analogs of $E(k)$ in fluid turbulence, are spread out over several decades in k . Therefore, we have demonstrated that, like fluid turbulence, spiral- and scroll-wave turbulence involves a wide range of spatial scales; $E_V(k)$ and $E_g(k)$ show approximate power laws in some range of k , but the exponents for these do not appear to be as universal as their counterparts in fluid turbulence. Even though there are diffusive terms in the equations we consider, they do not dissipate spiral or scroll waves completely because of the excitability of the medium. No external forcing is required to maintain these states of spiral- or scroll-wave turbulence. The only requirements are (i) a suitable initial condition and (ii) $L/\lambda \rightarrow \infty$ (or L/λ large enough in a practical calculation), where L is the linear size of the simulation domain and λ the wavelength of a plane wave in the excitable medium; the dimensionless ratio L/λ is a convenient, Reynolds-number-type control parameter (L is also used as a control parameter in a suitably scaled version of the Kuramoto-Sivashinsky equation [25]).

As we have mentioned above, 2D and 3D fluid turbulence are qualitatively different in so far as the former displays an inverse cascade of energy whereas the latter shows a forward cascade of energy. Spiral- and scroll-wave turbulence are not different in this manner. In both these cases there is the analog of a forward cascade: in 2D, large spirals break into small ones and in 3D, large scrolls also break into small ones. However, there are important differences between the spectral properties and PDFs that characterize the statistical properties of 2D, spiral-wave turbulence and 3D, scroll-wave turbulence. The differences can be gleaned by comparing our figures in Sec.III.A-B with their counterparts in Sec.III.C.

V. ACKNOWLEDGMENTS

We thank R. Majumder and A.R. Nayak for discussions, Council of Scientific and Industrial Research, University Grants Commission, Department of Science and Technology, and the European Cooperation in Science and Technology Action MP006 for support, and Supercomputing Education and Research Centre (IISc) for computational resources.

[1] D. Mozaffarian, E. J. Benjamin, A. S. Go et al, "Heart Disease and Stroke Statistics", —2015 Update, Circula-

tion 131 (2015);

[2] A.N. Zaikin and A.M. Zhabotinsky, "Concentration

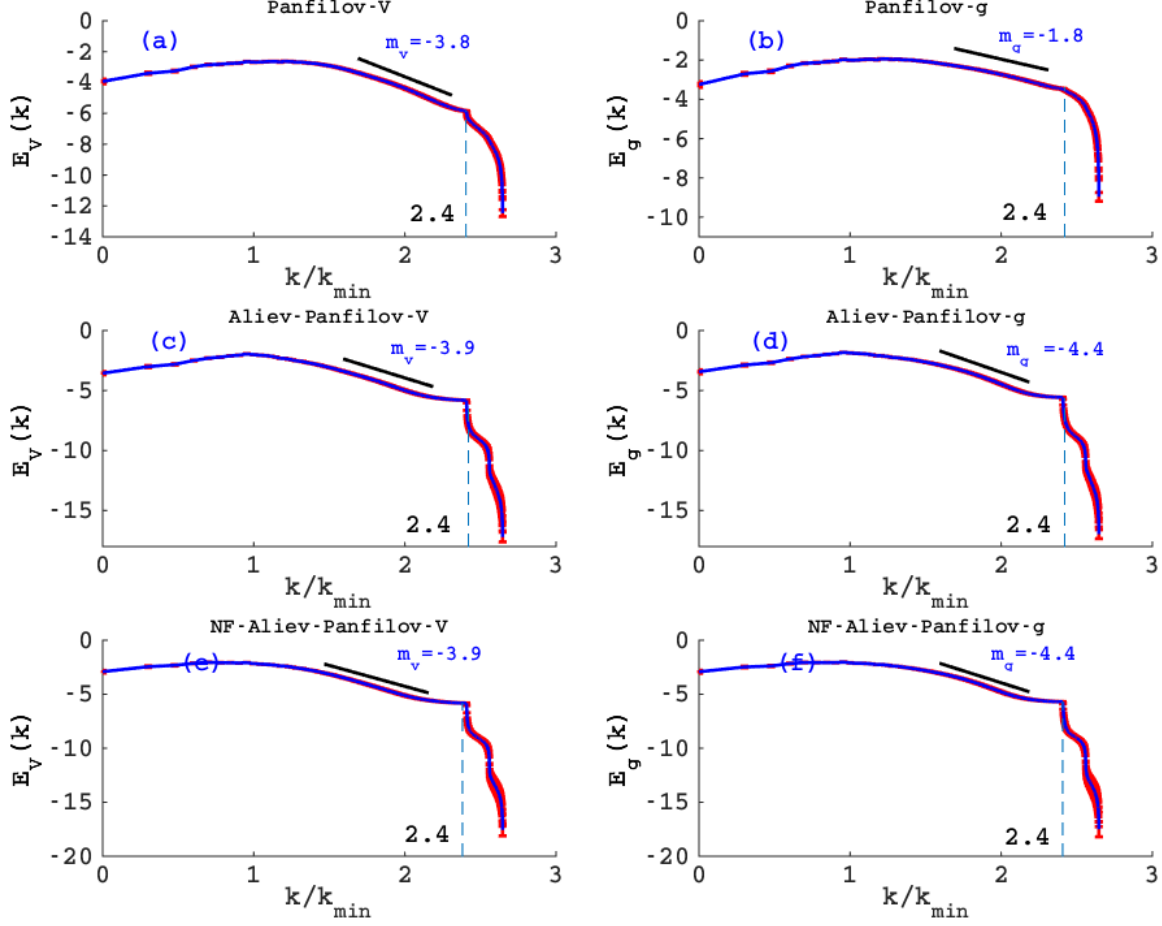


FIG. 23: Comparison of the spectra of E_V and E_g for 3D-scroll-wave turbulence in the three E models that we have studied. Here we show k/k_{min} on the horizontal axes; the peaks of the spectra occur at the same value of k , namely, $k/k_{min} \simeq 2.4$.

- wave propagation in two-dimensional liquid-phase self-oscillating system”, *Nature* **225**, 535 (1970); R.J. Field, L. Gyrgyi, Eds., *Chaos in Chemistry and Biochemistry* (World Scientific, Singapore, 1993); E. Ott, *Chaos in Dynamical Systems* (Cambridge University Press, Cambridge, UK, 1993); S.H. Strogatz *Nonlinear Dynamics and Chaos: With Applications to Physics, Biology, Chemistry and Engineering* (Addison-Wesley, Reading, Mass., USA 1994).
- [3] M. Bär and M. Eiswirth, ”Turbulence due to spiral breakup in a continuous excitable medium”, *Phys. Rev. E* **48**, R1635 (1993); M. Hildebrand, M. Bär and M. Eiswirth, ”Statistics of Topological Defects and Spatiotemporal Chaos in a Reaction-Diffusion System”, *Phys. Rev. Lett.* **75**, 1503 (1995); M. Bär, M. Hildebrand, M. Eiswirth, M. Falcke, H. Engel and M. Neufeld, ”Chemical turbulence and standing waves in a surface reaction model: The influence of global coupling and wave instabilities”, *Chaos* **4**, 499 (1994).
- [4] A. Pande and R. Pandit, ”Spatiotemporal chaos and nonequilibrium transitions in a model excitable medium”, *Phys. Rev. E*, **61**, 6448 (2000).
- [5] R. Imbihl, G. Ertl, ”Oscillatory Kinetics in Heterogeneous Catalysis”, *Chem. Rev.* **95**, (1995).
- [6] D.E. Clapham, ”Calcium signaling”, *Cell*, **80**, 259 (1995).
- [7] J.J. Tyson and J.D. Murray, ”Cyclic AMP waves during aggregation of Dictyostelium amoebae”, *Development* **106**, 421-426 (1989).
- [8] C. Weijer, ”Dictyostelium morphogenesis”, *Curr. Opin. Genet. Dev.* **14**, (2004).
- [9] G.R. Mines, ”On dynamic equilibrium in the heart”, *J. Physiol. (London)* **46**, 349382 (1913).
- [10] J.M. Davidenko, A.M. Pertsov, R. Salomonsz, W. Baxter, J. Jalife, ”Stationary and drifting spiral waves of excitation in isolated cardiac muscle”, *Nature* **355**, (1993).
- [11] A. T. Winfree, ”Electrical turbulence in three-dimensional heart muscle”, *Science*, 11 Nov 1994: Vol. 266, Issue 5187, (1991).
- [12] Noble Denis, ”The rise of computational biology”, *Nature Reviews Molecular Cell Biology* **3**, (June 2002).
- [13] A.V. Panfilov and P. Hogeweg, ”Spiral breakup in a modified FitzHugh-Nagumo model”, *Phys. Lett. A* **176**

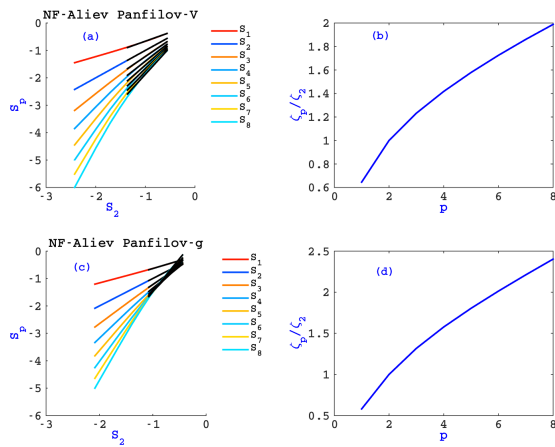


FIG. 24: ESS plots of structure functions of V and g for the case of 3D-scroll-wave turbulence in the negative-filament-tension regime.

- (1993); A.V. Panfilov, "Spiral breakup as a model of ventricular fibrillation", *Chaos* **8**, 57 (1998).
- [14] R. R. Aliev and A. V. Panfilov, "A simple two-variable model of cardiac excitation", *Chaos Solitons Fractals* **7**, 293 (1996).
- [15] E. Braunwald, *Heart Disease: A Textbook of Cardiovascular Medicine*, Vol.1, (Saunders International Edition (Fourth Ed) 1991).
- [16] T.K. Shajahan, S. Sinha and R. Pandit, Proceedings of Indian National Science Academy, **71 A**, 4757 (2005); R. Majumder, A.R. Nayak and R. Pandit, in O.N. Tripathi, *et al.* (eds.), *Heart Rate and Rhythm*, DOI 10.1007/978-3-642-17575-6-14, (Springer-Verlag, Berlin, Heidelberg, 2011) p 269.
- [17] NVIDIA CUDA Compute Unified Device Architecture: CUDA Programming Guide Version 3.0.
- [18] R.H. Clayton, O. Bernus, E.M. Cherry, H. Dierckx, F.H. Fenton, L. Mirabella, A.V. Panfilov, F.B. Sachse, G. Seemann, H. Zhang, "Models of cardiac tissue electrophysiology: progress, challenges and open questions", *Progress in Biophysics and Molecular Biology*, **104**, Issues 13, 22-48 (2011).
- [19] C. Luo and Y. Rudy, "A dynamic model of the cardiac ventricular action potential. II. Afterdepolarizations, triggered activity, and potentiation", *Circulation Research*, **74**, 1071-1097 (1994).
- [20] K.H.W.J. Ten Tusscher and A.V. Panfilov, "Cell model for efficient simulation of wave propagation in human ventricular tissue under normal and pathological conditions", *Phys. Med. Biol.*, **51**:6141-6156 (2006).
- [21] A.G. Kléber and Y. Rudy, "Basic mechanisms of cardiac impulse propagation and associated arrhythmias", *Physiol. Rev.* **84** 431-488 (2004).
- [22] T.K. Shajahan, A.R. Nayak and R. Pandit, "Spiral-Wave Turbulence and Its Control in the Presence of Inhomogeneities in Four Mathematical Models of Cardiac Tissue", *PLoS ONE* **4(3)**:e4738 (2009).
- [23] U. Frisch U 1996 *Turbulence: The Legacy of A N Kolmogorov* (Cambridge University Press, Cambridge, UK, 1996).
- [24] A N Kolmogorov, "On the degeneration of isotropic turbulence in an incompressible viscous fluid", *Dokl. Akad. Nauk SSSR* **30**, 301 (1941); **31**, 538 (1941).
- [25] C. Jayaprakash, F. Hayot and R. Pandit, "Universal properties of the two-dimensional Kuramoto-Sivashinsky equation", *Phys. Rev. Lett.* **71**, 12 (1993).
- [26] G. Boffetta and R.E. Ecke, "Two-Dimensional Turbulence", *Annu. Rev. Fluid Mech.*, **44**, 427 (2012).
- [27] T. Ishihara, T. Gotoh and Y. Kaneda, "Study of High-Reynolds Number Isotropic Turbulence by Direct Numerical Simulation", *Annu. Rev. Fluid Mech.* **41**, 165 (2009).
- [28] G. Sahoo, P. Perlekar and R. Pandit, "Systematics of the magnetic-Prandtl-number dependence of homogeneous, isotropic magnetohydrodynamic turbulence", *New J. Phys.*, **13** 0130363 2011.
- [29] G. Boffetta, A. Mazzino and A. Vulpiani, "Twenty-five years of multifractals in fully developed turbulence: a tribute to Giovanni Paladin", *J. Phys. A: Math. Gen.* **41**, 363001 (2008).
- [30] R. Pandit, P. Perlekar and S.S. Ray, "Statistical properties of turbulence: An overview", *Pramana - Journal of Physics*, **73** 157 (2009).
- [31] K.R. Sreenivasan and R.A. Antonia, "The phenomenology of small-scale turbulence", *Annu. Rev. Fluid Mech.* **29**, 435 (1997).
- [32] M. Lesieur, *Turbulence in Fluids*, Vol.84 of *Fluid Mechanics and Its Applications* (Springer, The Netherlands, 2008).
- [33] R. Fjørtoft, "On the Changes in the Spectral Distribution of Kinetic Energy for Twodimensional, Nondivergent Flow", *Tellus* **5**, 226 (1953).
- [34] R. H. Kraichnan, "Inertial Ranges in TwoDimensional Turbulence", *Phys. Fluids*, **10**, 1417 (1967).
- [35] C. Leith, "Diffusion approximation for two-dimensional turbulence", *Physics of Fluids*, **11**, 671 (1968).
- [36] G. K. Batchelor, "Computation of the energy spectrum in homogeneous two-dimensional turbulence", *Phys. Fluids Suppl. II*, **12**, 233 (1969).
- [37] P. Perlekar and R. Pandit, "Statistically steady turbulence in thin films: direct numerical simulations with Ekman friction", *New J. Phys.*, **11** 073003 (2009).
- [38] C. K Chan, D. Mitra and A. Brandenburg, "Dynamics of saturated energy condensation in two-dimensional turbulence", *Phys. Rev. E*, **85**, 036315 (2012).
- [39] R. Benzi *et al.*, "Extended self-similarity in turbulent flows", *Phys. Rev. E*, **48**, R29 (1993).
- [40] S. Chakraborty, U. Frisch and S.S. Ray, "Extended self-similarity works for the Burgers equation and why", *J. Fluid Mech.*, **649**, 275 (2010).
- [41] S. Alonso and A. Panfilov, "Negative Filament Tension at High Excitability in a Model of Cardiac Tissue", *Phys. Rev. Lett.*, **100**, 218101 (2008).
- [42]